applied optics

Optomechanical design of a wide-field auroral imager on Fengyun-3D

QUANFENG GUO,[1,*] BO CHEN,[1] SHIJIE LIU,[1] KEFEI SONG,[1] LINGPING HE,[1] FEI HE,[2] WEIGUO ZHAO,[1] ZHONGSU WANG,[1] LIHENG CHEN,[1] AND GUANGWEI SHI[1]

[1]Changchun Institute of Optics, Fine Mechanics and Physics, Chinese Academy of Sciences, Changchun 130033, China
[2]Institute of Geology and Geophysics, Chinese Academy of Sciences, Beijing 100029, China
*Corresponding author: guoqf@ciomp.ac.cn

Received 16 January 2022; revised 21 March 2022; accepted 23 March 2022; posted 24 March 2022; published 12 April 2022

We present the optomechanical design and development of a wide-field auroral imager (WAI) on board the satellite Fengyun-3D. The optomechanical system of the WAI features a combination of a large field of view and a single-axis scanning mechanism. The combination makes the WAI perform better than its counterparts in temporal resolution in a low Earth orbit. In-orbit tests have verified the survival of WAI in the launching vibration and space environment. It has functioned on-orbit since 2018, with a spatial resolution of ∼10 km at the nadir point, at a reference height of 110 km above the ionosphere.

https://doi.org/10.1364/AO.453949

1. INTRODUCTION

Auroral images have long been used as a monitor for solar and geomagnetic activities [1–6] because the aurora is caused by the interaction of the charged particles of solar wind and the magnetic tail with the molecules and atoms in the upper atmosphere. As an important part of the aurora, ultraviolet radiation is almost free of the complex background of the Earth's surface and the boundary layer atmosphere. Therefore, observing the aurora has become an important way of analyzing solar energy transmission and transformation, and monitoring the Earth's upper atmosphere and ionosphere. Other ultraviolet aurora research [7,8] has also set the atmospheric transmission model of ultraviolet radiation. Various data collected through auroral imaging have been extensively used for space weather forecasts and monitoring the space environment.

Since the first successful global aurora observation conducted by spin-scan auroral imaging (SAI) [9], on board the Dynamics Explorer 1 (DE-1) of the USA, in 1981, the exploration and application research for the ultraviolet aurora [10–19] has been carried out for nearly 40 years. The SAI adopts a Newtonian telescope and photomultiplier tube to perform a global auroral image from the polar regions (imaging altitudes of about 570 km to 3.65 R_E; $R_E = 6375$ km, the Earth's radius). It consists of four channels at 130.4 nm, 121.6 nm, 140–160 nm, and 140–170 nm with a field of view (FOV) 30 deg × 30 deg and an angular resolution less than 0.29 deg during an exposure time of 3 to 12 min. With the instrument, the information of hemispheric auroral distribution was captured for the first time. It is characterized by its mechanical structure for suppressing stray light with the super-polished mirror and special baffles, which effectively control the scattering light of the sunlit atmosphere. However, limited by its FOV, SAI spends 12 min scanning to gain a global picture of a hemispheric aurora. Due to the same limitation, the complete picture of the aurora taken by SAI is, in effect, spliced by picture pieces taken at different times within 12 min. It can be considered only as approximate to the hemispheric distribution of the aurora.

Two later developed auroral imagers on board the Viking satellite [14] and Freja satellite [16] have made significant improvements compared with the SAI of DE-1 in angular resolution and temporal resolution. The two imagers have similar layouts and parameters. To adapt to a wide range of operating temperature variations, they adopt two kinds of low expansion coefficient materials—graphite fiber epoxy composite (GFEC) and Zerodur glass—to make the imager housing and the mirrors. They also have an effective baffle system to prevent scattering from illuminated surfaces, and both have an inverse Cassegrain optical system with the same relative aperture number of F/1 and charge coupled device (CCD) detector with an enhanced array. To correct the distorted images and achieve rapid overall exposure, they are equipped with a curved micro-channel plate (MCP) and fiber array in the front of the CCD. The imagers have two channels, 134–180 nm (BaF_2 filter and CsI photocathode) and 123.5–160 nm (CaF_2 filter and KBr photocathode), with a FOV of less than 30 deg × 30 deg, angular resolution of 0.076 deg, and temporal resolution of 20 s/6 s. Due to the adoption of a CCD detector, the system requires real-time matching between the integration time of the CCD and the scanning time. The equipment complexity is, therefore, increased.

The ultraviolet imager (UVI) is another typical auroral remote sensor [17]. It is equipped on the POLAR spacecraft of the International Solar-Terrestrial Physics (ISTP) mission. UVI uses an off-axis optical system with three mirrors. Its excellent optical system can provide a remarkable pixel angular resolution of 0.03 deg. UVI operates on a high eccentric orbit (about 1.8 R_E to 9.0 R_E) and has three wavelength channels at 130.4 nm, 135.6 nm, and 140–180 nm. Although its FOV is only 8 deg, it can directly cover the entire auroral oval because the imaging distance can reach 8.0 R_E at apogee. The off-axis optical system with super polished mirrors and baffles makes it adequate in suppressing stray light. The instrument has also obtained many bands of auroral images, which significantly contributes to studying different auroral characteristics (e.g., proton auroral and electronic auroral). However, due to the high eccentric orbit, the special resolution of the global aurora of UVI is only 30 km.

A significant improvement in imaging performance has been made by a wideband imaging camera (WIC) [18] on the American satellite Imager for Magnetopause-to-Aurora Global Exploration (IMAGE), although its optical system is the same as those of the Viking and Freja. To minimize development risk, the WIC even chose a GFEC tube of Freja flight spare as its front optics housing. As the WIC works on the spinning satellite platform, it is designed with a time delay and integration (TDI) mode to ensure the resolution of the image. In the TDI image process, the distortion of each pixel is corrected in real time by a digital method. The method is also efficient in image translation and rotation. It avoids the risk of using vulnerable optical fiber components. WIC works at a wave band of 140–190 nm with a field angle of 17 deg × 17 deg, angular resolution of 0.18 deg (spatial resolution less than 100 km), temporal resolution of 2 min, and 256 × 256 pixels. WIC obtained many auroral images during a long operating period (2000–2005) during some magnetic breakups. However, the design of the MCP detector with a curved photocathode does not perform well in image quality.

Previous imagers did well in catching large-scale auroral images [20,21]. However, the necessity of studying the processes of the magnetosphere–ionosphere system calls for auroral imagers that can probe the small-scale structures of the auroral oval. Answering this call, the National Center for Space Weather, China Meteorological Administration (NCSW-CMA) started the aurora survey project [22] with FY3 serial satellites in 2012. The project planned to fill the above gap with the wide-field auroral imager (WAI). The WAI is the first auroral imaging instrument on the near-polar-orbiting Sun-synchronous orbit at 836 km. It was mounted on Fengyun-3D (FY-3D) and launched in 2017. It has observed the LBH band (140–180 nm) of far-ultraviolet (FUV) auroral radiation, which is radiated by N_2 molecules, and obtained the intensity distribution of the auroral oval [23]. This paper presents the optomechanical design of WAI and the finite element analysis (FEA) and tests that verify its feasibility.

2. SCIENTIFIC OBJECTIVES

The aurora usually appears in the sky of polar regions, including visible light and ultraviolet aurora. At the FUV band, significant auroral radiations include 121.6 nm (H Lyα), 130.0 nm (OI), 135.6 nm (OI), and 140–180 nm (N_2 LBH, molecular nitrogen, Lyman–Birge–Hopfield). N_2 LBH radiation intensity distribution is used to line out the auroral oval. By drawing the boundary of the auroral oval, the position of the geomagnetic substorm can be located. The solar extreme-ultraviolet (EUV) radiation flux can also be calculated by observing the auroral image.

Table 1. Parameters of WAI

Items	Specifications
FOV	130 deg × 130 deg
Wave bands	140 to 180 nm
Dynamic range	10^4
Sensitivity	$\geq$0.1 counts.s^{-1}.R^{-1}.pixel^{-1}
Pointing	$\leq$0.15 deg
Time delay	$\leq$2 min (1 frame)
Volume	$\leq$350 mm × 300 mm × 250 mm
Mass	$\leq$15 kg
Reliability	$\geq$0.85

WAI on board the FY-3D satellite is designed to capture N_2 LBH (140–180 nm) auroral images for studying the auroral substorm and its relation to solar activity. It starts in-orbit scanning as long as the satellite flies over the polar regions and captures FUV images every 2 min until the satellite flies out of the polar region. Its optomechanical design considers various factors, including the FOV, stray light suppression, vibration in the transfer and flight phase, space radiation environment, thermal environment, and volume and mass. The WAI is designed to obtain global FUV images for at least four years. The major parameters of WAI are shown in Table 1.

3. OPTICAL SYSTEM

A. Optical Design

Theoretically, there are several alternative design schemes for a large FOV of 130 deg × 130 deg.

1. *Gazing Refractive Lenses*

A refractive optical system with a FOV at 130 deg × 130 deg can be realized by splicing four lenses of 70 deg × 70 deg FOV with an angular resolution of 0.1 deg. However, reliable optical material that works as an EUV band for connecting the lenses is rare. Although the crystal materials such as LiF, MgF_2, and CaF_2 can be used as EUV bands, they are prone to deliquescence and are challenging to process. In addition, their refractive indices vary enormously from 140–180 nm, which dramatically raises technical difficulties and risks.

2. *Two-Axis Scanning with Small FOV Lenses*

A large FOV of 130 deg × 130 deg can be achieved by two-axis scanning and image splicing of simple optical systems with a small FOV. However, there are several technical barriers in carrying out this scheme. First, the complexity of the scanning mechanism makes it hard to secure a service life of more than four years. Second, it is difficult to sew the relatively simple auroral images together. Third, this system requires a long exposure time, which exceeds the maximum time resolution allowed. Taking an optical system with a 10 deg × 10 deg FOV as an example, when its shortest exposure time of 5 s is satisfied, a single scanning cycle needs at least about 13 min, which fails to meet the requirement of temporal resolution of 2 min.

3. *Single-Axis Scanning with Two Wide-Field Reflective Lenses*

An alternative option is a spliced off-axis reflective lens with two 68 deg × 10 deg FOVs, making a wide FOV of 130 deg × 10 deg. The lens scans along the field direction of 10 deg to achieve 130 deg × 130 deg FOV with an angular resolution of 0.8 deg. The wide-field lens scans along the orbital path to obtain an auroral image of the entire polar region when the satellite flies over the polar region.

Compared with the first two schemes, scheme 3 shows its advantages in fewer scanning axes and better temporal resolution. Therefore, scheme 3 is adopted in the overall design of the WAI. The design of the optical system is shown in Fig. 1. The single optical lens uses an off-axis reflective optical system with four mirrors, and the 68 deg × 10 deg FOV of the optical system is obtained by the primary convex mirror [24]. The pupil is set in the shape of a rectangle. The rectangular pupil is conducive to achieving a reasonable system structure layout and effectively suppressing stray lights. At the Nyquist frequency (6.7 lp/mm), the minimum modulation transfer function (MTF) of the optical system is 0.76 in the full FOV, and the average MTF value of the optical system is more than 0.82, which meets the requirement of the optical system MTF. The optical design results show that the system has high image quality and sound stray light suppression.

B. Mirrors and Filter

The WAI uses an off-axis reflective optical system consisting of four mirrors and an aft filter. The layout of the mirrors and the filter is shown in Fig. 1. Zerodur material is used as the mirror's substrate because of its low thermal expansion coefficient.

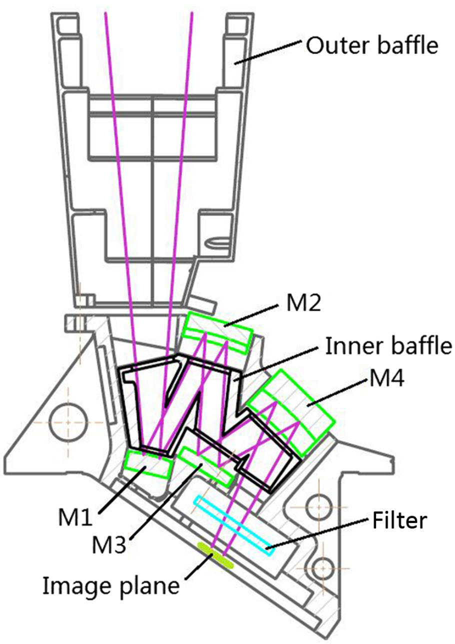

Fig. 1. WAI optical layout.

Barium fluoride material is used for the filter because of the good bandpass transmission at 140–180 nm.

According to the optical design requirements, the optomechanical structure of the lens and detector should be stable enough and easy to align and adjust. Each mirror has a small reflective area and an off-axis value. The tight position and low surface tolerance of the optical elements require a narrow error range to ensure good optical performance.

C. Baffle Design

As the imager is designed to operate nonstop, suppression of stray light is an important part of the optomechanical design of WAI. With an off-axis reflective structure and effective baffle system, the imager is excellent in suppressing stray light and scattered sunlight. The outer shading and inner blocking baffles can eliminate stray light outside the FOV, as shown in Fig. 1. To suppress the stray light caused by structural scattering, a particular painting and sufficient vanes with knife edges are used for the baffle system to ensure stray light suppression performance.

4. MECHANICAL DESIGN

A. Mechanical Structure

In designing the support system, several factors have to be considered. First, the support system should be a compact, lightweight structure to meet the mass requirement. At the same time, the mechanical design also needs to meet the requirement of convenience in alignment and testing [25]. The scanning mechanism should work for more than four years and survive in mechanical and thermal environments from Earth to space.

The core components of the WAI are the scanning mechanism and wide-field optical system. The weight and height of the center of mass of the scanning part are minimized to improve structural stability, so only the lenses, the detecting unit, the rotating frame, and the scanning mechanism are left in the scanning part. The cable between the lens and electronic box is set through the hole of the hollow shaft to minimize bending damage and improve the reliability of the wired connection and signal transmission. In addition, the fabrication and alignment process of the mirror support structure, the base support, U-shaped frame, hall sensor mount, and wiring scheme are also optimized to fit with the scanning system.

The mechanism is driven directly by a stepping motor to meet the requirements of a rotation accuracy of 0.1 deg, high rotation reliability over 10E7 circles, and no less than 1.1 deg per second of scanning speed.

WAI has a volume of 600 mm × 300 mm × 605 mm. It consists of the base support, U-shaped frame, lens assembly, motor, assistant support, and scanning and positioning assembly (see its structure model in Fig. 2).

B. Lens Assembly

The lens assembly consists of two identical optical lenses and a frame. To adjust the gravity center of the rotating body, the two lenses are symmetrically mounted on the lens assembly frame, as shown in Fig. 3. Two independent optical axes of the two lenses are in the same plane with an angle of 65 deg. Mounting the

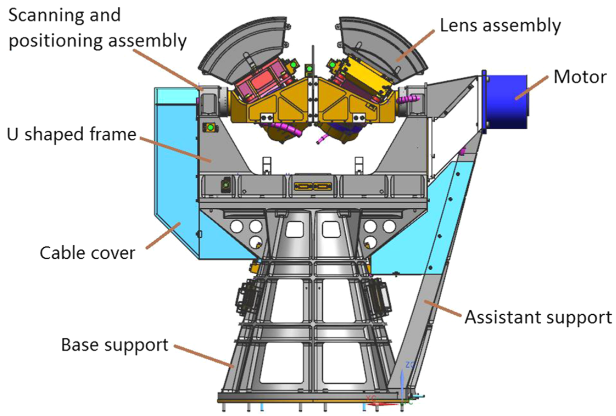

Fig. 2. WAI structure model.

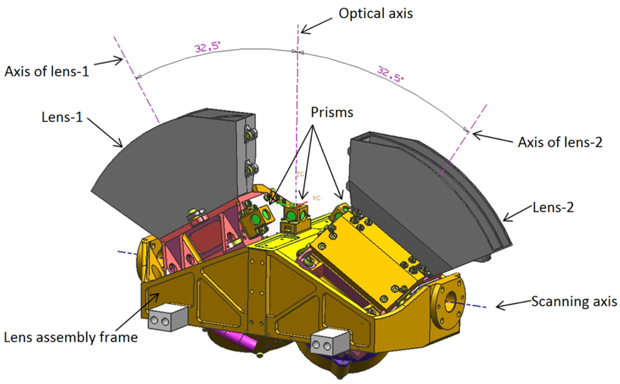

Fig. 3. Layout of the lens assembly.

two sets of lenses through the hole of the lens assembly frame reduces the moment of inertia and eccentricity of the rotating object. The mounting surfaces of the two lenses form an angle of 115 deg on the lenses frame, and the two optical axes are also in the same plane with the rotating axis of the frame. This stitching design ensures the instant view of 133 deg × 10 deg. The two sets of lenses and the assembly frame are aligned with three calibrating prisms, which facilitates the alignment of the three axes.

1. *Lens Structure*

The lens structure is designed based on the layout of the off-axis reflective optical system. All four mirrors are mounted on a frame structure. According to the optical requirements, the optomechanical structure of the lens and the detector of the WAI should be stable enough to maintain the image quality and pointing direction. The lens has stringent tolerances because of the small reflecting areas of mirrors and the off-axis optical system. Therefore, it is necessary to maintain a high position precision to ensure good optical performance. The lens structure and the focal plane assembly (FPA) are shown in Fig. 4. The lens assembly comprises the lens support, four mirrors, baffles, a filter, and the FPA.

As the main component of the lens structure, the lens frame is designed as a one-piece unit and machined by a single piece of 7075 aluminum. The high thermal conductivity of the

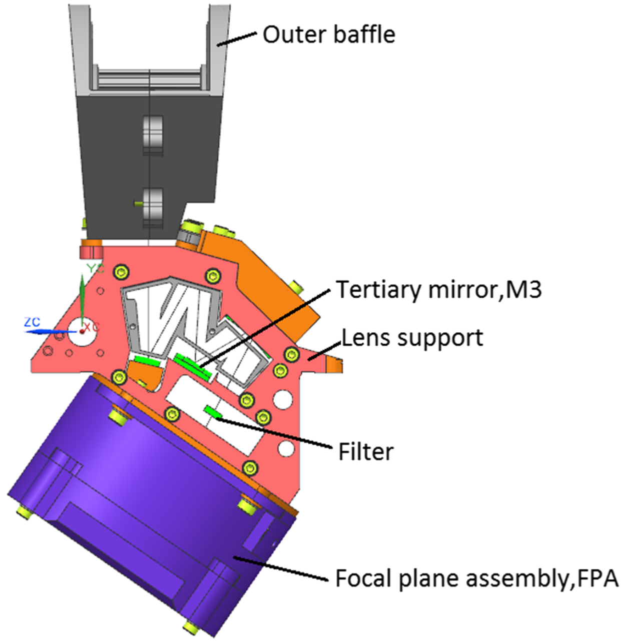

Fig. 4. Diagram of the lens assembly.

aluminum alloy helps reduce the temperature gradient of mirrors and ensures the thermal stability of the focal plane. The one-piece design of the lens frame makes it possible to meet the requirement of assembly precision and thermal stability. The assembly precision requires a surface flatness of 0.01 mm and an average roughness of 0.0016 mm. Exceptionally high precision is required in the assembly of the tertiary mirror because its position is taken as a baseline in the mounting of other mirrors and focal planes, as shown in Fig. 4. The accuracy of the angle between the mirrors is achieved by the machining process to simplify the mirror position adjustment in the optical alignment process. The mounting position of the FPA makes it easy for optical alignment and adjustment, and the thermal stability of the focal plane is ensured by mounting the FPA at the end of the lens frame through a thermal insulating pad.

2. *Focal Plane Assembly*

The FPA of WAI consists of a photon-counting detector, a fore magnifier, a group of high-voltage resistors, an aluminum detector housing, a rear cover, and a shield plate between the magnifier and the resistors. The detector is mounted in the housing through a flange. The resistors are welded on the rear of the detector to ensure good electrical insulation. The safety distance between the welding points and other faces is more than 4 mm. A removable side cap is designed for future check or service of the high-voltage resistors on the detector housing face. Following the resistors, the shield plate, fore magnifier, and two rear cover parts are mounted in the housing. Additionally, the rear cover is designed in two parts to meet the needs of the testing and mounting of electrical connectors. The design guarantees the connection between the electrical connector and the fore magnifier when the cover is removed.

The layout of the FPA and its shields is shown in Fig. 5. The position of the detector and the focal plane can be adjusted by

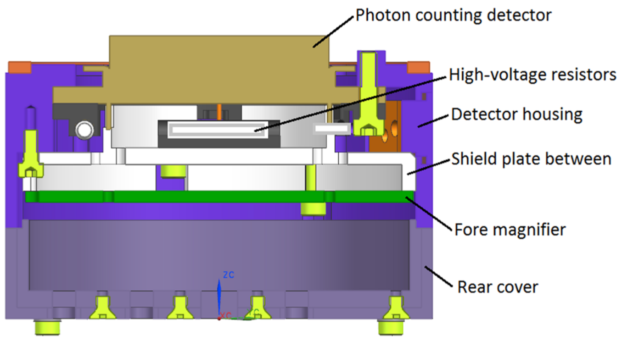

Fig. 5. Layout of the FPA and electromagnetic shields.

fixing the insulating pad, which is between the FPA and the lens frame.

The fore magnifier circuit is located at the rear of the detector and is directly connected to the detector anode. The electronic cells and circuits are required to comply with the requirements of the electromagnetic shield. A shield plate is adopted between the fore magnifier circuit and the detector to ensure the circuit is in an enclosed electromagnetic shield. The thickness of the shield wall is 3 mm, as required by the electromagnetic shield.

C. Mechanism

The WAI is an integration of mechanical structures and electronic assemblies. The mechanical system is driven by a stepping motor because it has the advantages of simple structure, smooth movement, and high reliability. The transmission mechanism is shown in Fig. 6.

As illustrated in Fig. 6, there is no gearbox in the transmission link. Direct driving can simplify the transmission link but requires a high torque on the motor. As required by the mechanism load, a motor that can bring a 2 N.m torque with a volume of Φ85 mm × 70 mm and weight of 2.0 kg is selected.

The gravity center of the stepping motor is closer to the U-shaped frame, which makes it stable in a vibration environment. Therefore, it is directly mounted on the face of the U-shaped frame, which is the primary support for the motor. As the weight of the motor is large, mechanical auxiliary support between the motor and the base is adopted to enhance the rigidity of the whole structure. The additional support serves to ensure the mechanical properties of the imager structure.

The transmission mechanism comprises the U-shaped frame, lens assembly, Hall sensors, shaft, stepping motor, coupling between the shaft and stepping motor, and their bearings. The direct driving structure is shown in Fig. 7.

The rotating system comprises a fixed end and an adjustable end of the shaft, a coupling, and the stepping motor. The fixed end of the shaft is mainly composed of a pair of angular bearings and a rod. The outer shell of angular bearings is fixed with the

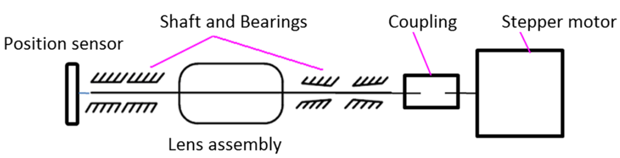

Fig. 6. Transmission illustration of the mechanism.

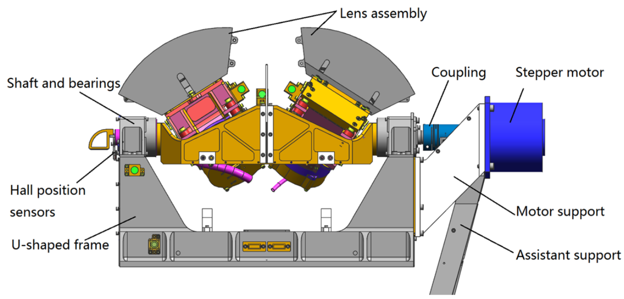

Fig. 7. Direct driving structure with a stepping motor.

mount. The shaft can rotate with the inner shell of angular bearings but cannot move along the axis direction. At the adjustable end, the ball bearings and the other rod comprise the compensatory shaft. The ball bearings and their housing can move relative to each other to compensate for the axial deformation of the rotating system subject to environmental effects.

Two important components, motor support and assistant support, are used to ensure the stability of the heavy motor. Besides supporting the motor, the motor support ensures the translation stiffness of the motor. The assistant support is mainly used to increase the support stiffness of the motor [26].

As for the rotation accuracy of the transmission mechanism, it is undertaken mainly by the stepping motor. The stepping motor is driven in a subdivision way. A subdivision, 0.0225 deg, is 1/20 of one step of the motor. The rotation error in one step of the motor is less than 0.045 deg, ensuring the transmission mechanism has a maximum rotation angle error of no more than 0.0675 deg, which meets the pointing requirement.

5. ANALYSIS

A. Thermal Analysis

Thermal distortions of mirror surfaces can severely degrade the image, making the thermal analysis of lens assembly one of the most crucial ground tests.

The first factor that needs to be controlled to avoid thermal distortion is the range of temperature changes. The lens frame, mirrors, and filter are made of aluminum, Schott Zerodur, and barium fluoride, and their coefficients of linear thermal expansion (CTEs) are $23 \times 10^{-6}\ \mathrm{K}^{-1}$, zero, and $18.4 \times 10^{-6}\ \mathrm{K}^{-1}$, respectively. The operating temperature of the imager ranges from 20 to 40 deg Celsius. According to the optomechanical design, the influence of temperature variation on image quality can be analyzed by optical design software. The optical analysis results show that the MTF value varies in a narrow range when the temperature is between 20 and 40 deg Celsius. Therefore, the design guarantees the stability of the focal position and image quality without adjusting the focus within the operating temperature range of 20 to 40 deg Celsius.

The second factor is the effect of the temperature gradient. Despite applying thermal isolation, thermal gradients still exist in the system. Thermal gradients may deform the shape of the mirror surface and optomechanical structure. The lens frames are made of 7075 aluminum, an alloy with good thermal conductivity to minimize the thermal gradient of each mirror. The simulation test results show the biggest thermal gradient

Table 2. Material Properties of Mechanical Structure

Material	Density ρ(g/cm^3)	Young's ModulusE (MPa)	Poisson's Ratio ν	Parts
Zerodur	2.53	90,600	0.17	Mirrors
BaF_2	4.89	53,200	0.343	Filter
4J32	8.1	141,000	0.25	Substrate of mirror
7075	2.7	69,000	0.32	Support and lens structures
40Cr	7.85	206,000	0.25	Shafts
9Cr18	7.7	200,000	0.3	Bearings
Ti6Al4V	4.4	114,000	0.29	Base of bearings

of the single mirror is about 0.2 deg Celsius, and the thermal gradient of the lens assembly is less than 3 deg Celsius. The CTE of Zerodur mirrors is nearly zero, and their thermal deformation is less than 1 nm (peak–valley value), which has a negligible effect on image quality [27].

B. Dynamic Response Analysis

To check the dynamic stiffness of WAI and verify the overall mechanical resistance of the structure, it is necessary to simulate the mechanical properties using FEA.

The mechanical properties of the structural material of WAI are shown in Table 2.

Before analysis, a finite element model is established based on the structural entity model and material properties. The mechanical requirements of environmental test specifications are used as the input for the mechanical simulation analysis.

The natural frequencies and response modes of the imager are shown in Table 3 and Fig. 8. As shown in Table 3, WAI has the first natural frequency of 106.3 Hz, higher than the required level of 100 Hz.

C. Random Vibration Response Analysis

The response analysis of random vibration is carried out according to the requirements of identification. The identification requirements are illustrated in Tables 4 and 5, showing the acceleration response to the random vibration load. The response value is denoted in the form of root mean square.

The results show that the maximum acceleration response of the motor is 38.71 g_{rms}, which indicates that the structure can withstand random vibrations.

Table 3. Natural Frequencies of Wide-Field Auroral Imager

Direction	Natural Frequency (Hz)	Description
X	106.3	Translation along *x* axis and rotating around *z* axis
Y	147.9	Translation along *y* axis
Z	368.7	Translation along *z* axis

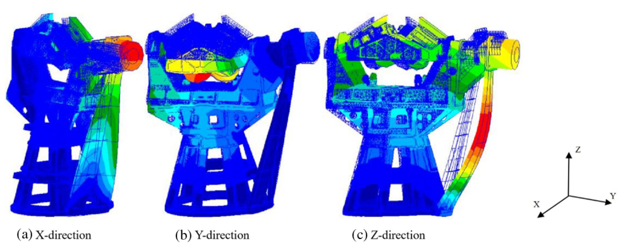

Fig. 8. Frequency response modes of WAI.

Table 4. Identification Requirements of Random Vibration

Frequency (Hz)	Test Conditions	Acceleration (g_{rms}, root mean square)	Direction	Period
200–100	+3 dB/oct	8.6	*X*/*Y*/*Z*	2 min
100–600	0.09 g^2/Hz			
600–2000	−9 dB/oct			

Table 5. Results of Acceleration Response under Random Loads

Position	Response to *X* Load /g_{rms}	Response to *Y* Load /g_{rms}	Response to *Z* Load /g_{rms}
Joint holes of U-shaped frame	21	20.07	24.53
End of U-shaped frame	20.32	23.59	14.85
Center of lens frame	17.52	22.08	25.22
Mounting interface of motor	16.12	20.47	23.39
Outer end of motor	26.07	23.09	38.71
Bottom of detectors	21.69	22.22	32.9
Center of base support	9.30	10.10	8.40

6. TESTS

A. On-Ground Tests

To evaluate the performance of WAI during a test or conditioning, there are many types of tests that need to be carried out. Some tests of response to sinusoidal and random loads have been carried out to verify the analysis results and obtain the real response to dynamic excitation from vibration. The imager is installed on the table of the vibration system during mechanical tests. The fixing of the imager and the test result of the fundamental frequency are shown in Fig. 9.

The fundamental frequency of the imager is 113.578 Hz, which is in line with the simulation result. After the vibration, shock, and acceleration tests, the fundamental frequency changes less than 5%, which shows that the imager has sufficient structural rigidity.

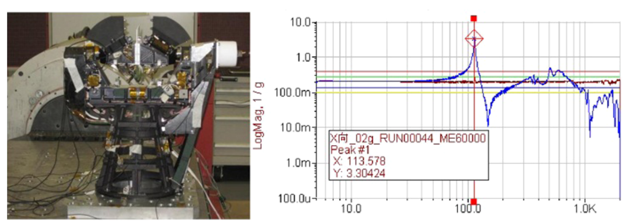

Fig. 9. (left) Fixing of the imager and (right) test result of the fundamental frequency.

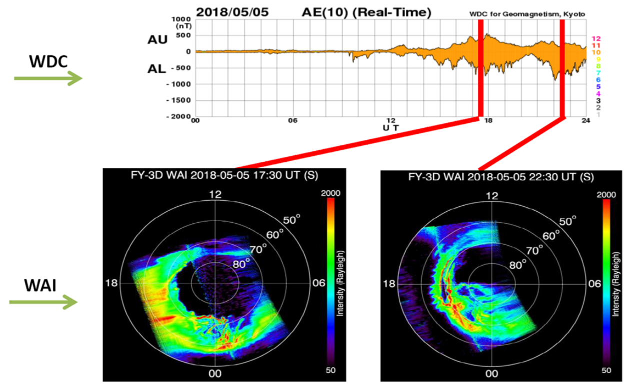

Fig. 10. Auroral images captured by WAI and WDC.

Based on the resulting frequencies and vibrations of analysis and tests, we draw the following conclusions: the imager has a fundamental frequency greater than 100 Hz, which meets the requirement; the change of fundamental frequency is less than 5%; the imager passed the mechanical tests.

B. In-Orbit Tests

In the orbital phase, WAI operates in a near-polar-orbiting Sun-synchronous orbit at ∼830 km. According to the optical parameter, WAI can get a spatial resolution of 10 km on the auroral reference sphere or ionosphere at the height of 110 km. Fig. 10 illustrates the auroral images of 140–180 nm captured at 17:30 UT and 22:30 UT on 25 May 2018, by WAI (in nadir mode) and the corresponding data from the World Data Center for Geomagnetism, Kyoto (WDC), during a geomagnetic storm [28]. The auroral images captured by WAI are consistent with the data of WDC, which proves that WAI performs well in orbit.

7. CONCLUSION

The optomechanical design of WAI is featured with a pair of joint lenses and a single-axis scanning mechanism. This design feature gets a large FOV of 130 deg × 130 deg and enables WAI to obtain a global auroral image with single scanning in the expected four-year lifetime. Compared with its counterparts, it has a simple but more reliable mechanical structure, works with a high temporal resolution, and, at the same time, provides images of a higher spatial resolution. WAI's stable in-orbit functioning also verifies the designing reliability. Data collected by WAI are consistent with those of the WDC.

Funding. National Natural Science Foundation of China (41674155, 41774152).

Acknowledgment. Great support has been provided by the Fengyun3 satellite team and the WAI instrument team throughout the optomechanical design of WAI. The WAI image data were processed and provided by the ground application system at NSMC, CMA.

Disclosures. The authors declare no conflicts of interest.

Data availability. Data underlying the results presented in this paper are available in Ref. [28].

REFERENCES

1. D. J. Strickland, J. R. Jasperse, and J. A. Whalen, "Dependence of auroral FUV emissions on the incident electron spectrum and neutral atmosphere," J. Geophys. Res. Space Phys. **88**, 8051–8062 (1983).
2. R. R. Meier, "Ultraviolet spectroscopy and remote sensing of the upper atmosphere," Space Sci. Rev. **58**, 1–185 (1991).
3. G. A. Germany, M. R. Torr, D. G. Torr, and P. G. Richards, "Use of FUV auroral emissions as diagnostic indicators," J. Geophys. Res. Space Phys. **99**, 383–388 (1994).
4. G. A. Germany, D. G. Torr, P. G. Richards, M. R. Torr, and S. John, "Determination of ionospheric conductivities from FUV auroral emissions," J. Geophys. Res. Space Phys. **99**, 23297–23305 (1994).
5. C. E. Keffer, M. R. Torr, M. Zukic, J. F. Spann, and J. Kim, "Radiation damage effects in far-ultraviolet filters, thin films, and substrates," Appl. Opt. **33**, 6041–6045 (1994).
6. G. Johnsen, A. Zolich, S. Grant, R. Bjørgum, J. H. Cohen, D. McKee, T. P. Kopec, D. Vogedes, and J. Berge, "All-sky camera system providing high temporal resolution annual time series of irradiance in the Arctic," Appl. Opt. **60**, 6456–6468 (2021).
7. G. P. Anderson, J. H. Chetwynd, J. M. Theriault, P. Acharya, and E. P. Shettle, "MODTRAN2: suitability for remote sensing," Proc. SPIE **1968**, 514–525 (1993).
8. D. J. Strickland, J. S. Evans, J. E. Bishop, T. Majeed, P. M. Shen, R. Link, and R. E. Huffman, "Atmospheric ultraviolet radiance integrated code (AURIC): current capabilities for rapidly modeling dayglow from the far UV to the near IR," Proc. SPIE **2831**, 184–199 (1996).
9. L. A. Frank, J. D. Craven, K. L. Ackerson, M. R. English, R. H. Eather, and R. L. Caravillano, "Global auroral imaging instrumentation for the dynamics explorer mission," Space Sci. Instrum. **5**, 369–393 (1981).
10. C. D. Anger, T. Fancott, J. McNally, and H. S. Kerr, "ISIS- II scanning auroral photometer," Appl. Opt. **12**, 1753–1766 (1973).
11. E. H. Rogers, D. F. Nelson, and R. C. Savage, "Auroral photography from a satellite," Science **183**, 951–952 (1974).
12. K. Hirao and T. Itoh, "Scientific satellite Kyokko (EXOS-A)," Solar Terr. Env. Res. Jpn. **2**, 148–152 (1978).
13. C. I. Meng and R. E. Huffman, "Ultraviolet imaging from space of the aurora under full sunlight," Geophys. Res. Lett. **11**, 315–318 (1984).
14. C. D. Anger, S. K. Babey, A. L. Broadfoot, R. G. Brown, L. L. Cogger, R. Gattinger, J. W. Haslett, R. A. King, D. J. McEwen, J. S. Murphree, E. H. Richardson, B. R. Sandel, K. Smith, and J. A. Vallance, "An ultraviolet auroral imager for the Viking spacecraft," Geophys. Res. Lett. **14**, 387–390 (1987).
15. T. Oguti, E. Kaneda, M. Ejiri, S. Sasaki, A. Kadokura, T. Yamamoto, K. Hayashi, R. Fujii, and K. Makita, "Studies of aurora dynamics by aurora-TV on the Akebono (EXOS-D) satellite," J. Geomag. Geoelectr. **42**, 555–564 (1990).
16. J. S. Murphree, R. A. King, T. Payne, K. Smith, D. Reid, J. Adema, B. Gordon, and R. Wlochowicz, "The Freja ultraviolet imager," Space Sci. Rev. **70**, 421–446 (1994).
17. M. R. Torr, D. G. Torr, M. Zukic, R. B. Johnson, J. Ajello, P. Banks, K. Clark, K. Cole, C. Keffer, G. Parks, B. Tsuratani, and J. Spann, "A far ultraviolet imager for the international solar-terrestrial physics mission," Space Sci. Rev. **71**, 329–383 (1995).
18. S. Mende, H. Heetderks, H. Frey, M. Lampton, S. Geller, R. Abiad, O. Siegmund, A. Tremsin, J. Spann, H. Dougani, S. Fuselier, A. Magoncelli, M. Bumala, S. Murphree, and T. Trondsen, "Far ultraviolet imaging from the IMAGE spacecraft. 2. Wideband FUV imaging," Space Sci. Rev. **91**, 271–285 (2000).
19. A. B. Christensen, L. J. Paxton, S. Avery, J. Craven, G. Crowley, D. C. Humm, H. Kil, R. R. Meier, C. I. Meng, D. Morrison, B. S. Ogorzalek, P. Straus, D. J. Strickland, R. M. Swenson, R. L. Walterscheid, B. Wolven, and Y. Zhang, "Initial observations with the global ultraviolet imager (GUVI) in the NASA TIMED satellite mission," J. Geophys. Res. Space Phys. **108**, 1451 (2003).
20. K. M. Laundal and N. Østgaard, "Asymmetric auroral intensities in the Earth's northern and southern hemispheres," Nature **460**, 491–493 (2009).
21. D. S. Han, Y. Nishimura, L. R. Lyons, H. Q. Hu, and H. G. Yang, "Throat aurora: the ionospheric signature of magnetosheath particles penetrating into the magnetosphere," Geophys. Res. Lett. **43**, 1819–1827 (2016).

22. C. Tu, R. Schwenn, E. Donovan, E. Marsch, J. Wang, L. Xia, Y. Zhang, K. W. Team, and K. W. Team, “Space weather explorer–the KuaFu mission,” Adv. Space Res. **41**, 190–209 (2008).
23. X. Zhang, B. Chen, F. He, *et al.*, “Wide-field auroral imager onboard the Fengyun satellite,” Light Sci. Appl. **8**, 47 (2019).
24. M. Laikin, *Lens Design*, 4th ed. (CRC Press, 2007).
25. J. Hosek, V. Havran, S. Nemcova, J. Bittner, and J. Cap, “Optomechanical design of a portable compact bidirectionaltexture function measurement instrument,” Appl. Opt. **56**, 1183–1193 (2017).
26. Z. Wang, Q. Guo, F. Jiang, B. Chen, Q. Wu, and G. Wang, “Stiffness design of cantilevered structure with space optics load,” Optik **184**, 330–338 (2019).
27. H. B. Yang, L. H. Chen, Y. Li, H. W. Liu, and F. He, “Thermal design and verification of transmission filter for wideangle aurora imager,” Opt. Precis. Eng. **22**, 3019–3027 (2014).
28. Data Analysis Center for Geomagnetism and Space Magnetism, Kyoto University, “World Data Center for Geomagnetism: real-time AE index,” 2018, http://wdc.kugi.kyoto-u.ac.jp/ae_realtime/201805/index_20180505.html.